Control of Stripe-Domain-Wall Magnetization in Multilayers Featuring Perpendicular Magnetic Anisotropy

Ruslan Salikhov,[1,*] Fabian Samad,[1,2] Benny Böhm,[2] Sebastian Schneider,[3] Darius Pohl,[3] Bernd Rellinghaus,[3] Aladin Ullrich,[4] Manfred Albrecht,[4] Jürgen Lindner,[1] Nikolai S. Kiselev,[5,†] and Olav Hellwig[1,2]

[1] *Institute of Ion Beam Physics and Materials Research, Helmholtz-Zentrum Dresden-Rossendorf, Bautzner Landstrasse 400, Dresden 01328, Germany*

[2] *Institute of Physics, Chemnitz University of Technology, Reichenhainer Strasse 70, Chemnitz 09107, Germany*

[3] *Dresden Center for Nanoanalysis, cfaed, Technische Universität Dresden, Dresden 01069, Germany*

[4] *Institute of Physics, University of Augsburg, Universitätsstrasse 1, Augsburg 86159, Germany*

[5] *Peter Grünberg Institute and Institute for Advanced Simulation, Forschungszentrum Jülich and JARA, Jülich 52425, Germany*

(Received 21 April 2021; revised 29 June 2021; accepted 28 July 2021; published 9 September 2021)

We report on the controlled switching of domain-wall (DW) magnetization in aligned stripe-domain structures, stabilized in $[\mathrm{Co}(0.44\ \mathrm{nm})/\mathrm{Pt}(0.7\ \mathrm{nm})]_X (X = 48, 100, 150)$ multilayers with perpendicular magnetic anisotropy. The switching process, induced by an external magnetic field, is monitored by measuring the evolution of the in-plane magnetization. We show that the remanent in-plane magnetization originates from the polarization of the Bloch-type DWs. With micromagnetic simulations, we reveal that the reversal of the DW polarization is the result of the emergence and collapse of horizontal Bloch lines within the DWs at particular strengths of the external magnetic field, applied opposite to the DW polarization. Our findings are relevant for DW-based magnonics and bubble-skyrmion applications in magnetic multilayers.

DOI: 10.1103/PhysRevApplied.16.034016

I. INTRODUCTION

Magnetic multilayers (MLs) with perpendicular magnetic anisotropy (PMA) are synthetic materials with highly tunable properties. The accurate control of the magnetic properties in these heterostructures is realized by adjusting their design parameters, e.g., the ML periodicity, ferromagnetic sublayer thickness, and number of repeats. Over the years, these materials have found wide use in many fields, such as data-storage technology [1,2], nonvolatile logic [3], spintronics [4,5], magnonics [6–9], and biotechnology [10].

There is particular interest concerning magnetic MLs with a high quality factor, $Q = K_u/K_d$, which represents the ratio between the PMA energy density at in-plane saturation, K_u, and the magnetostatic energy density at out-of-plane saturation, $K_d = (1/2)\mu_0 M_s^2$, where μ_0 is the vacuum magnetic permeability and M_s is the saturation magnetization. In MLs with $Q \ll 1$, the ground state is a single-domain state with magnetization lying in the plane of the film. In the case of strong PMA ($Q \gtrsim 1$), the competition between long-range magnetostatic interactions and short-range exchange interactions results in the formation of magnetic domains with "up" and "down" magnetization, which can form labyrinth patterns, aligned stripe domains, or cylindrical magnetic bubble domains [11,12]. The control of such magnetic states by external stimuli, such as a magnetic field, an electric current, or temperature, offers vast perspectives for fundamental research and applications.

MLs with PMA have been reconsidered recently as host materials for bubble skyrmions, i.e., bubble domains with defined domain-wall (DW) chirality in the presence of interfacial Dzyaloshinskii-Moriya interaction (IDMI). The IDMI is induced by asymmetric interfaces, such as Ir/Fe/Co/Pt or Pt/Co/Ir [3,13].

The well-established MLs with symmetric interfaces, such as Co/Pt or Co/Pd, still offer rich perspectives. A high spin-orbit-torque efficiency in combination with the robust thermal stability can be realized using metallic MLs for spintronic applications [14–16]. On the other hand, aligned stripe-domain structures stabilized in these MLs have been suggested as media for spin-wave propagation [6–9,17]. This opens up perspectives for current-controlled

*r.salikhov@hzdr.de
†n.kiselev@fz-juelich.de

reconfigurable magnonic devices, operated at high frequency and with low power consumption [17].

The direction of the domains can be reconfigured using an external magnetic field or electric current [17–19]. Besides the stripe-domain direction, the magnetization orientation inside the DWs can be another degree of freedom to control the characteristics of the spin waves localized in the DWs [6–9]. In this work, we investigate the concept and report on internal switching of the DW polarity, induced by in-plane magnetic fields, in Co/Pt MLs with strong PMA. The switching is accompanied by the emergence of horizontal Bloch lines (HBLs) inside the DWs of aligned stripe domains. The concept of a HBL has been well established for garnet films and other bubble materials [20,21]; however, it has not yet been reported for magnetic MLs.

Using vibrating-sample magnetometry (VSM), we study the magnetization reversal inside the DWs by performing in-plane minor-hysteresis-loop series with the field applied parallel to the stripe-domain long axis. These measurements reveal a cascade of transitions leading to a steplike evolution of the in-plane remanent magnetization as a function of the previously applied field. We argue that the observed behavior in our system generally applies for PMA MLs with symmetric interfaces. This argument is supported by the reproducibility of such a cascade of transitions in a sample series with different thicknesses. Our study further comprises experimental measurements with magnetic force microscopy (MFM) and Lorentz transmission electron microscopy (LTEM), as well as micromagnetic simulations, which allow us to reveal fine details of the magnetization-reversal processes inside individual domain walls.

The paper is organized as follows. We first outline the sample preparation and experimental techniques, including the method for the stripe-domain alignment. Then we discuss the in-plane magnetization minor loops and the remanent-magnetization behavior as a function of the previously applied field, along with supporting MFM and LTEM images. Finally, we show the results of micromagnetic simulations and provide a comprehensive picture of the magnetization-reversal processes and the role of HBLs. These results contribute to a fundamental understanding of DW magnetic polarization and switching in PMA MLs, inspiring their research and applications with symmetric and asymmetric interfaces.

II. EXPERIMENTAL DETAILS

The $[(\mathrm{Co}(0.44\ \mathrm{nm})/\mathrm{Pt}(0.7\ \mathrm{nm})]_X$, $X = 48$, 100, 150 ML films are fabricated at room temperature by dc-magnetron sputter deposition at 0.4 Pa Ar atmosphere in an ultrahigh-vacuum system (ATC 2200, from AJA International Inc.). We use Si substrates with a 100-nm-thick thermally oxidized (SiO_2) layer. Prior to the multilayer deposition, a 1.5-nm Ta layer is grown for adhesion purposes. A subsequent 5-nm- or 20-nm-thick Pt buffer serves as a seed layer for inducing a preferred (111) texture of the Co/Pt MLs, which supports larger and more uniform PMA. The ML samples are finally capped by 2-nm Pt to avoid surface oxidation. Magnetic measurements are performed at ambient temperature on a commercial Microsense EZ7 vibrating sample vector magnetometer (VSM), equipped with an electromagnet, and a goniometer for angle-dependent measurements. For magnetic domain imaging, we use a Bruker Dimension Icon magnetic force microscope. All MFM images are recorded at room temperature and zero magnetic field.

The DW-magnetization imaging is performed using LTEM. For the LTEM experiments, the $[(\mathrm{Co}(0.44\ \mathrm{nm})/\mathrm{Pt}(0.7\ \mathrm{nm})]_{48}$ ML is fabricated on a silicon nitride TEM grid using a 5-nm Pt buffer layer in order to reduce absorption. The LTEM investigation is performed with a JEOL NEOARM TEM (JEM-ARM200F), operated at 200-keV beam energy, in the Lorentz mode. Images are taken with a Gatan OneView camera. No further treatment (such as plasma cleaning) is applied to the samples.

The aligned stripe-domain states in all the samples are prepared using a specific ac-demagnetization (ACD) routine, namely by alternating the magnetic field direction parallel to the sample surface, with subsequent reduction of the field amplitude from 1600 mT down to 2 mT in 2% steps. This routine brings the sample into a fully demagnetized state, which is characterized by zero remanence. The saturation magnetization of all samples is measured using the VSM and calculated to be $M_s = 0.77 \pm 0.07$ MA/m. The PMA constant is determined from the in-plane saturation field of a ML with a structure identical to that of the samples investigated here but with smaller $X = 12$ (yielding a square out-of-plane hysteresis). We obtain $K_u \approx 0.6\ \mathrm{MJ/m^3}$, leading to the value $Q \approx 1.6$; therefore, the strong stripe-domain criteria are met for all samples investigated here [20–23].

III. RESULTS

Before discussing our results in detail, we briefly recall studies from the late 1980s, when the magnetic domain structures in garnet films were intensively investigated for magnetic bubble-memory applications [24–27]. Back then, it was demonstrated that in high-Q films, the magnetization inside the DWs between aligned stripe domains can be switched by applying an in-plane magnetic field. Moreover, it was shown that the switching of the DW polarity does not affect the magnetic structure and stability of the stripe domains [24–27]. Here, we show that a similar switching process takes place in magnetic MLs. However, the mechanism of the switching is different to the one proposed in Refs. [24,25].

Magnetic hysteresis loops for the [Co(0.44 nm)/Pt(0.7 nm)]$_X$ MLs are presented in Figs. 1(a) and 1(b) for $X = 48$ and $X = 100$, respectively. Both samples exhibit a similar magnetic response that is typical for MLs with PMA [28–30]. The magnetization measured in the out-of-plane geometry shows easy-axis behavior, as expected for MLs with $Q \gtrsim 1$. At remanence, the system evolves into a labyrinth-type domain structure with almost equal widths of "up" and "down" domains, shown in the top-left inset of Fig. 1(a). In the in-plane geometry, the magnetization shows hard-axis behavior, however, with nonzero remanence [see the bottom-right insets in Figs. 1(a) and 1(b)]. There, the magnetic domains evolve to a mixed state consisting of short and elongated stripe domains in combination with some bubble domains [top-left inset of Fig. 1(b)], when the magnetic field is decreased from saturation to zero. The normalized remanent magnetization $m_r = M_r/M_s$ (M_r being the magnetization at zero field) decreases slightly with X (see Table I), indicating a weak dependence on the sample thickness.

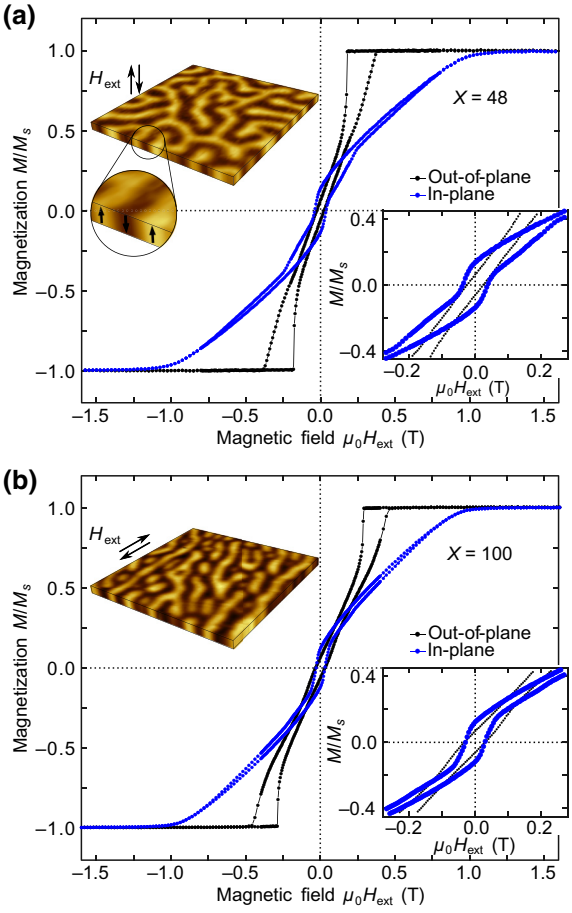

FIG. 1. Magnetic hysteresis loops measured with magnetic field applied perpendicular (black circles) and parallel (blue circles) to the [Co(0.44 nm)/Pt(0.7 nm)]$_X$ multilayer surface for (a) $X = 48$ and (b) $X = 100$. The bottom insets show an enlarged view of the corresponding hysteresis loop at small magnetic fields. The top insets are schematic illustrations adapted from approximately 2μm $\times$ 2μm-sized MFM images for the multidomain state at remanence, $H_{ext} = 0$, after (a) out-of-plane and (b) in-plane magnetic saturation.

TABLE I. The total magnetic film thickness t, the normalized remanent magnetization, $m_r = M_r/M_s$, the DW saturation field, $\mu_0 H_{cr1}$, the DW magnetic activation field, $\mu_0 H_{cr2}$, the averaged stripe-domain width, λ, and the effective DW width, Δ, for [Co(0.44 nm)/Pt(0.7 nm)]$_X$ multilayers with $X = 48$, 100, and 150.

	$X = 48$	$X = 100$	$X = 150$
t	55 nm	114 nm	171 nm
m_r	0.135	0.12	0.09
$\mu_0 H_{cr1}$	240 mT	200 mT	250 mT
$\mu_0 H_{cr2}$	50 mT	40 mT	37 mT
λ	80 ± 5 nm	91 ± 5 nm	115 ± 5 nm
Δ	22 ± 2 nm	22 ± 2 nm	20 ± 2 nm

In the following, we demonstrate that the remanent magnetization measured parallel to the stripe-domain long axis originates from the magnetization inside of Bloch-type DWs. As shown in Fig. 2(a), after the ACD protocol, the samples exhibit parallel stripe domains aligned along the magnetic field direction. In contrast to the case where we reduce the in-plane field directly from saturation to zero (Fig. 1), we now observe a vanishing remanent magnetization [see the state marked by "(I)" in Fig. 2(d)].

The aligned stripe-domain structure in Fig. 2(a) exhibits a domain period of 160 ± 10 nm. Figure 2(b) shows the LTEM magnetic DW contrast for these stripe domains and Fig. 2(c) is the corresponding fast Fourier transformation (FFT). The irregular contrast of the LTEM image and the broad peaks in the FFT indicate a random alignment of the in-plane Bloch-wall component of different DWs (along the two possible directions), which is expected after ACD.

In a second step, we then apply a moderate in-plane field along the stripe-domain direction in order to align all the Bloch components of the DWs into one of the two possible orientations and then reduce the field back to zero. We now pick up a significant remanent in-plane moment (m_r = 0.135) along the stripe-domain direction, as is visible for state "(II)" in Fig. 2(d). The MFM image, shown in Fig. 2(e), has not changed in any significant way and the domains are still in a fully aligned state with the period of 160 ± 10 nm. However, the LTEM image [Fig. 2(f)] now shows, at normal incidence of the electrons—where we are only sensitive to the projected in-plane magnetic induction and hence to in-plane Bloch-wall components—a much narrower stripe pattern with a well-defined period of 75 ± 5 nm [Fig. 2(g)]. This confirms that all the Bloch components of the DWs are now pointing in the same direction and thus result in a period of 75 ± 5 nm, which coincides with half of the domain-pattern period obtained from the

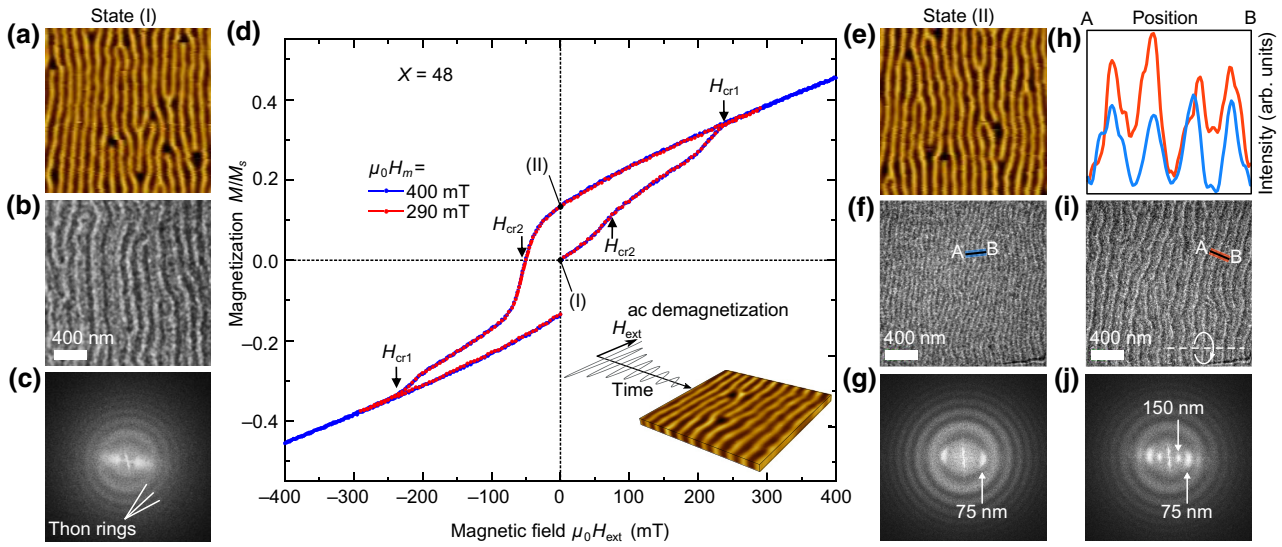

FIG. 2. (a) A MFM image of the aligned stripe-domain state and (b) the LTEM magnetic contrast with a corresponding (c) FFT of the magnetization inside the DWs in the $[Co(0.44\ nm)/Pt(0.7\ nm)]_{48}$ sample. Initially, the sample is in an in-plane ACD state. (d) Minor hysteresis loops up to 290 mT (red line) and 400 mT (blue line). The field is applied parallel to the stripe domains, starting from the demagnetized state (I). The states (I) and (II) marked in the loops correspond to the domain states presented in (a) and (b) and then (e) and (f), respectively. (e) A MFM image of stripe domains recorded at zero field after exposing the demagnetized sample to a field of 300 mT, (f) the corresponding LTEM magnetic contrast of the DWs, and (g) its FFT. (i) The LTEM contrast and (j) the corresponding FFT for a sample region inclined with respect to the normal incidence of the electrons. The tilt axis is schematically depicted by the dashed line in (i). In that case, the LTEM contrast emerges from the out-of-plane domains and gets superimposed onto the LTEM contrast from the DWs. (h) The intensity amplitudes of the LTEM contrasts in (f) (blue line) and in (i) (red line). All MFM and LTEM images are recorded at zero magnetic field and at room temperature but at different locations on the sample.

MFM images (within the error bars determined by the FFT peak broadening).

Figure 2(i) shows the magnetic contrast from an inclined region of the membrane with respect to the electron beam. In that case, electrons penetrate the sample with an angle to the surface normal and thus experience some additional deflection due to the in-plane magnetic induction components of the domains themselves. In such a geometry, we now see both periods, the 150-nm period from the domains superimposed on the 75-nm period from the "artificially aligned" DWs [Fig. 2(j)]. This is also clearly visible in the comparison of the LTEM image line profiles of normal incidence [Fig. 2(f), blue] versus inclined incidence [Fig. 2(i), red] regions, displayed in Fig. 2(h). Indeed, the red curve exhibits an additional sinusoidal 150-nm modulation as compared to the blue curve. The original ac-demagnetized sample does not show any visible periodicity of 75 nm. As a result, we can conclude that the nonzero remanent in-plane moment measured along the stripe direction originates from the polarized DW magnetization.

Having confirmed that the remanent in-plane magnetization originates from the Bloch-type DW polarization, we study the characteristics of the DW magnetic switching. In the following, if not otherwise mentioned, we present and discuss data for in-plane magnetic fields applied parallel to the stripe-domain long axis. The minor-loop series for MLs with $X = 48$, 100, and 150 are displayed in Figs. 3(a)–3(c), respectively. With an increasing magnetic field, the magnetization increases and reveals a hysteretic behavior with an opening between ascending and descending branches of the minor hysteresis loops. As soon as the maximum magnetic field, H_m, in the minor-loop series overcomes H_{cr1} [$\mu_0 H_{cr1} = 240$ mT for $X = 48$; see Figs. 2(d) and 3(a)], the descending branch of the loop shows constant remanence, which is independent of H_m. The positive slope above H_{cr1} results from the continuous and reversible rotation of the magnetization inside the domains toward the external magnetic field direction [24,25,29,31,32]. All samples show switching from a zero-point demagnetized state to a finite remanent-magnetization state at $H_m > H_{cr1}$. The critical field H_{cr1} and the remanent magnetization for all MLs are summarized in Table I.

For small fields $H_m \leq H_{cr2}$ ($\mu_0 H_{cr2} = 50$ mT for $X = 48$), on the other hand, the magnetization shows a linear and reversible response to the field. Accordingly, the remanent moment remains zero, as is also visible in Fig. 3(d), which presents the plot of m_r as a function of H_m. The remanent magnetization for all samples shows a characteristic double-step behavior as a function of H_m until H_m overcomes the critical field H_{cr1} [see the plot in

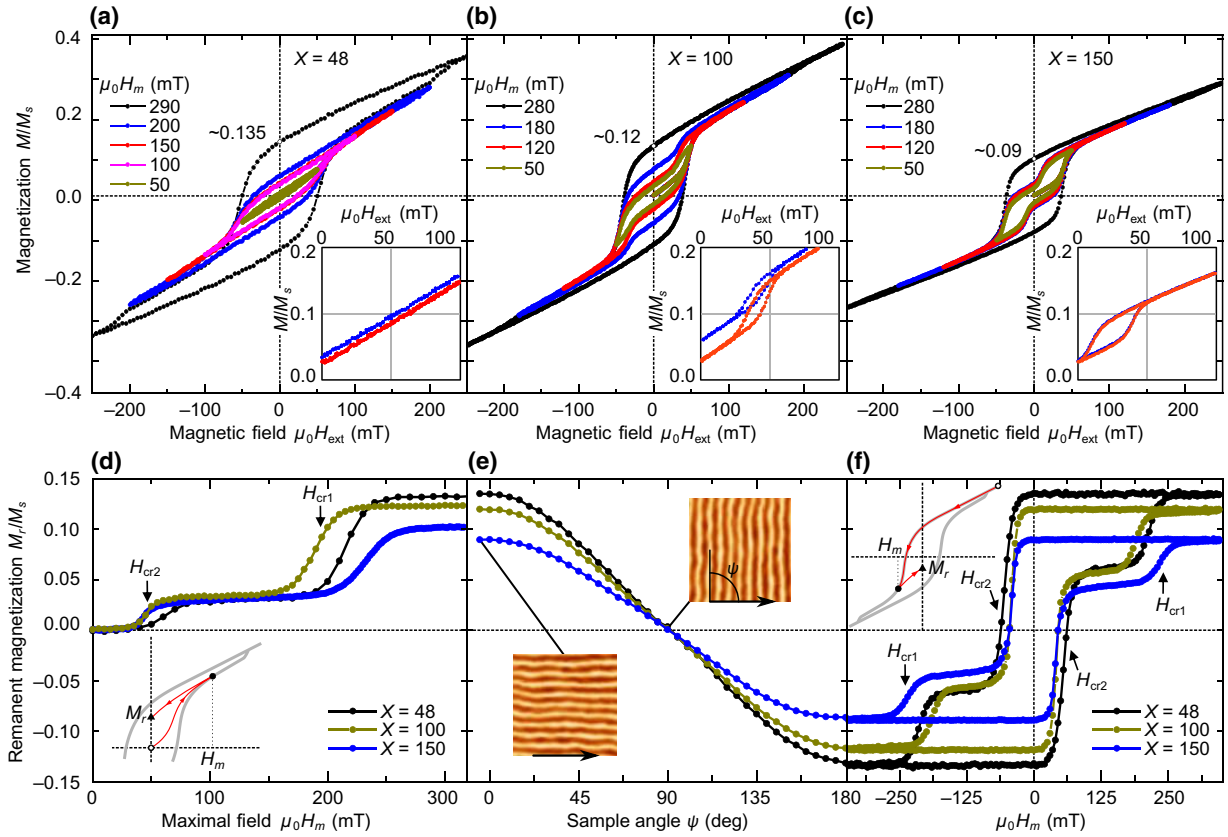

FIG. 3. The magnetic minor-loop series with different maximum magnetic fields, H_m, for $[\mathrm{Co}(0.44\ \mathrm{nm})/\mathrm{Pt}(0.7\ \mathrm{nm})]_X$ multilayers with (a) $X = 48$, (b) $X = 100$, and (c) $X = 150$. The field is applied parallel to the long axis of the stripe domains, which are created by previous in-plane ACD. The insets in (a)–(c) present the DW-magnetization behavior as a function of the magnetic field varied through the inflection point associated with the critical field H_{cr2}. Note that with increasing X, the minor loops exhibit an opening. (d) The normalized remanent magnetization as a function of the previously applied field, $\mu_0 H_m$, starting from the aligned stripe state stabilized by ACD. The inset shows in detail the initial state after ACD (hollow circle), the state at maximum field (solid circle), and the final state at remanence (triangle), which is displayed in the main plot of (d). (e) The angular dependence of the in-plane remanent magnetization of the aligned stripe domains, where $\psi = 0$ corresponds to an angle to the direction parallel to the stripes. The black arrow in the insets indicates the direction along which the remanent magnetization is measured. (f) The normalized remanent magnetization as a function of the maximum applied magnetic field, $\mu_0 H_m$, varied between $+300$ mT and -300 mT and back. In contrast to (d), in these measurements, the initial state is an in-field state (see the hollow circle in the inset). Note that all data points in (d), (e), and (f) are taken at zero magnetic field and that all three graphs have identical y-axis scales.

Fig. 3(d)]. Another plateau appears at $H_{cr2} < H_m < H_{cr1}$ [Fig. 3(d)], corresponding to approximately 20%–30% of the maximum remanent moment. This plateau represents an intermediate stable DW-polarization remanent state. The associated energy barriers for the DW-magnetization reversal in the vicinity of H_{cr1} and H_{cr2} are modeled and discussed below. Note that the irreversibility point in the major in-plane magnetic hysteresis loops in Figs. 1(a) and 1(b) occurs at a higher field of approximately 720 mT, showing that domain deformation requires larger magnetic field energies as compared to DW switching.

We further investigate the direction of the total net in-plane remanent magnetization by measuring m_r for different in-plane angles ψ between the stripe-domain long axis and the VSM pick-up coil axis [see Fig. 3(e)]. Prior to this measurement, the sample is brought into a stripe-domain state by ACD and then a field of 300 mT (which is above H_{cr1} for all samples) is applied along the stripe axis. For $\psi = 0°$, the moment is measured parallel to the previously applied field, which gives the maximum signal from the polarized DWs. For $\psi = 90°$, on the other hand, the signal vanishes. This shows that the net in-plane moment in our system is indeed parallel to the stripe DWs and can be identified as the DW Bloch components polarized in one direction by the previously applied magnetic field protocol.

So far, we have discussed the DW-magnetization behavior starting from the fully demagnetized state after the ACD protocol to the polarized state. Figure 3(f) plots the remanent magnetization for $\mu_0 H_m$ varied between -300 mT and $+300$ mT; thus the plot represents full

magnetization reversal inside the DWs. The double-step behavior is also evident, with critical fields (H_{cr1} and H_{cr2}) identical to those defined in Fig. 3(d) and given in Table I. The DW magnetization changes sign and shows a plateau at $H_{cr2} < H_m < H_{cr1}$, however, this time the magnetic polarization reaches about 40%–50% of its maximum.

The minor hysteresis loops for our ML series show a systematic trend with the sample thicknesses (X): the loop opening in between the two critical field values H_{cr2} and H_{cr1} is narrowing down with increasing ML thickness X, as seen when comparing minor-loop series for $X = 48$, 100, and 150 in Figs. 3(a)–3(c). Furthermore, the DW magnetization of $X = 100$ and 150 samples shows partial exchange-springlike behavior until the magnetic field exceeds H_{cr1}. The exchange-spring behavior has been reported for two-dimensional domain walls in hard-soft bilayer exchange-spring magnets [33–35], where the point of irreversibility is only reached when the DW penetrates into the hard layer. In thick (above-1-μm) garnet films, this behavior has been clearly demonstrated and referred to as a first jump in the double-jump magnetization reversal of the stripe DWs [25].

Since the in-plane remanent magnetization is attributed to the polarization of the DW Bloch component, it becomes possible to estimate an effective DW width (corresponding to a linear Bloch DW profile without Néel caps), Δ, for the aligned stripe-domain configuration. A simple equation can be used [23,29]:

$$\Delta = 2\lambda m_r. \tag{1}$$

The stripe-domain width, λ, is determined from the MFM images. The effective DW width, presented in Table I, is independent of the ML thickness. This is expected from the models for stripe domains in high-Q materials with thicknesses above the characteristic critical thickness [23,36]. Since the DW width does not change with the sample thickness, magnetic MLs with a larger domain periodicity should exhibit smaller remanent magnetization. This explains why m_r decreases with X in our sample series.

IV. MICROMAGNETIC SIMULATIONS

To explain the physical nature of the magnetization curves and shed some light on the process taking place inside the domain wall during the magnetization reversal, we utilize micromagnetic simulations performed with the MUMAX3 code [37]. The main results of the numerical simulations are summarized in Fig. 4. The simulated domain has the shape of a cuboid with thickness $L_z = 52.8$ nm, which is approximately the magnetic thickness of the sample with $X = 48$. In the x-y plane, the sample has a rectangular shape with the size fitting the equilibrium period of the stripe domains, $L_x = L_y = 2\lambda$, and contains two DWs. We use periodic boundary conditions in the x-y plane and assume that the magnetic field is parallel to the x axis [see Fig. 4(a)]. In the simulations, we use the experimentally estimated values for the saturation magnetization, $M_s = 0.775$ MA/m, and the out-of-plane anisotropy constant, $K_u = 0.6$ MJ/m^3. We assume that the exchange coupling between Co layers is weaker than the direct exchange within the layer, such that the overall Heisenberg exchange becomes anisotropic. In the micromagnetic approximation, the corresponding energy density term can be written as

$$w_{ex} = A \sum_i \left[\left(\frac{\partial m_i}{\partial x} \right)^2 + \left(\frac{\partial m_i}{\partial y} \right)^2 + k_{IEC} \left(\frac{\partial m_i}{\partial z} \right)^2 \right], \tag{2}$$

where the summation runs over $i = x, y, z$. The constant A is the exchange stiffness in the plane of the film and $\mathbf{m} = \mathbf{M}/M_s$ is the magnetization unit-vector field. The unitless constant k_{IEC} in Eq. (2) defines the strength of the exchange coupling between Co layers across the Pt layers. For exchange-decoupled layers, $k_{IEC} = 0$, and in the approximation of isotropic media, $k_{IEC} = 1$. We estimate the constants A and k_{IEC} from the fit of the experimental data for the domain size and critical fields H_{cr1} and H_{cr2}. Figure 4(f) shows the dependence for the equilibrium domain size, λ, as a function of the exchange stiffness, A, calculated for two limiting cases $k_{IEC} = 0$ and 1. We find the best agreement with the experimentally estimated $\lambda = 80$ nm for $X = 48$ at $A = 8$ pJ/m, which represents a reasonable value for Co/Pt MLs [38]. The dependence of λ on k_{IEC} is too weak to allow for an estimation of k_{IEC}. Instead, we perform a series of simulations for magnetization-reversal curves with different k_{IEC}. The representative magnetization curve for $k_{IEC} = 0.2$ is shown in Fig. 4(g). The profile of the magnetization inside the left (L) and right (R) DWs across the thickness are depicted in Figs. 4(b)–(e) for the different in-plane field values; the corresponding states are also marked on the magnetization curves [Fig. 4(g)]. In the initial demagnetized state, the two DWs have opposite magnetization in the Bloch part of the DW [Fig. 4(b)]. The averaged in-plane component of magnetization projected onto the x axis is zero in this case. With increasing H_{ext}, the magnetization inside the DW is rotated, tending to be aligned with the field direction. For small fields $H_{ext} < H_{cr2}$, the profile of the magnetization changes insignificantly and is not shown here. At the external field approaching H_{cr2}, the magnetization profile changes abruptly [Fig. 4(c)]. In the right DW (R), with the magnetization in the middle plane pointing opposite to the external field, we observe the formation of a well-localized area with strongly twisted magnetization which we refer to as a HBL [20]. The emergence of the HBL leads to an abrupt increase of the magnetization in the direction of the applied magnetic field, which results in the bending of the magnetization curve at $H_{ext} = H_{cr2}$. Since the state with

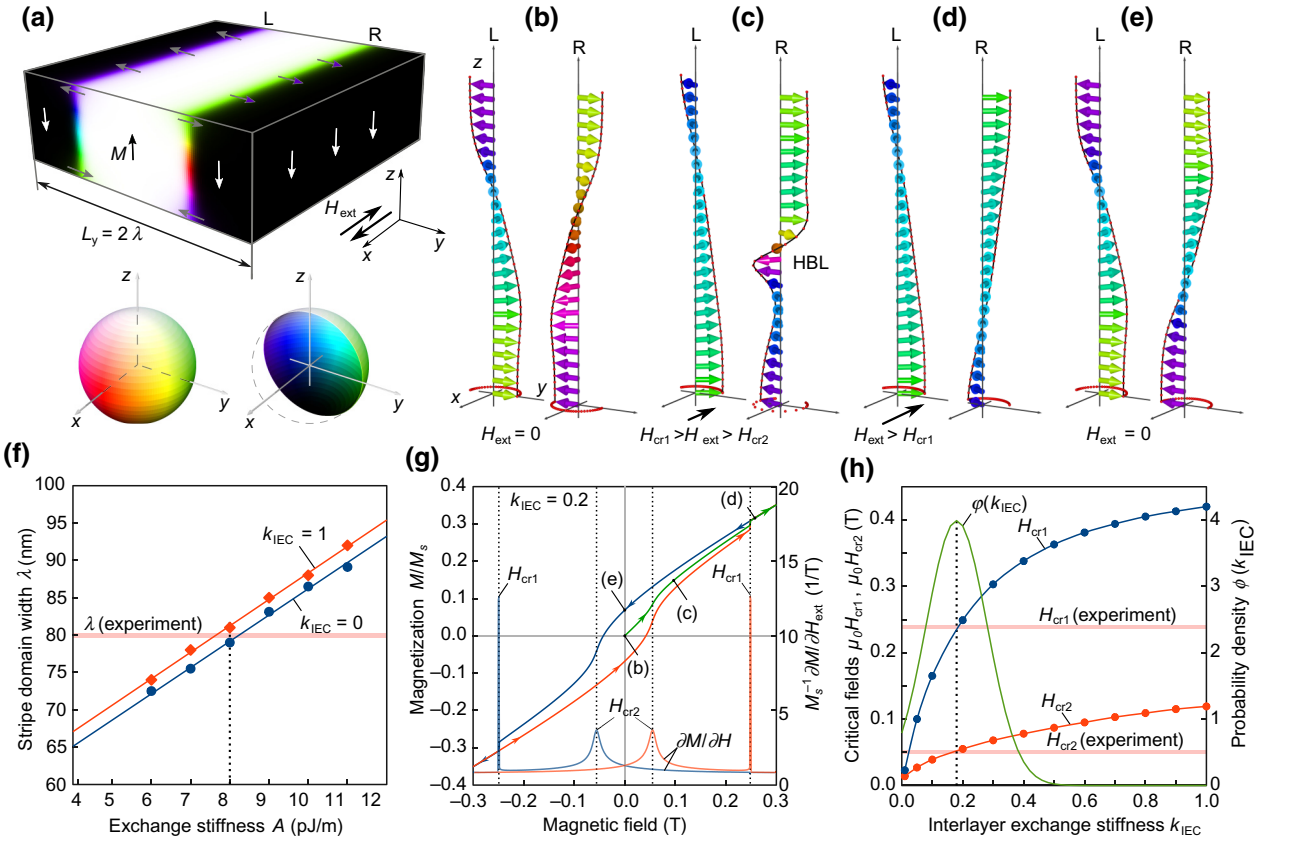

FIG. 4. (a) The simulated domain and equilibrium magnetization distribution at zero external field for the $X = 48$ ML. The unit-vector field for magnetization is represented with the color code displayed by the inset below. (b)–(e) The magnetization along the thickness of the sample inside the left (L) and the right (R) domain walls [see (a)] at different external magnetic fields applied antiparallel to the x axis. (f) The equilibrium stripe-domain width calculated for different values of exchange stiffness constant A and coefficient of interlayer exchange coupling, k_{IEC} [see Eq. (2)]. (g) The representative magnetization curve calculated on the domain shown in (a) by energy minimization at each field. The green line is the virgin magnetization curve starting from the demagnetized state depicted in (a). The blue and the red lines are the descending and ascending branches of the minor magnetization loop, respectively. The peaks of the differential susceptibility $\partial M/\partial H$ shown for descending (blue) and ascending (red) branches indicate the two transitions. (h) The dependence of the critical fields H_{cr1} and H_{cr2} on the interlayer exchange coupling. The vertical dashed line indicates the optimal value, $k_{IEC} = 0.18$, at which the theoretical fields match the experimental ones. The green curve shows a normal distribution for k_{IEC} with mean $k_{IEC} = 0.18$ and assuming a variance $\sigma^2 = 0.01$.

the HBL has a strong magnetization gradient, its energy is much higher than the energy of the DW with magnetization aligned with the field. There is always a critical field H_{cr1} above which the HBL abruptly switches to the field-aligned state [Fig. 4(d)].

According to our observations, the switching occurs via nucleation of a pair of singularities—Bloch points with opposite index. The Bloch points run along the domain wall in opposite directions, because the area between them represents the field-aligned state with lower energy. The switching process finishes when the Bloch points reach the physical boundaries of the sample or meet other Bloch points with opposite index and annihilate. The dynamics of the Bloch points and the mechanism of their nucleation and/or annihilation are beyond the scope of this work and will be discussed elsewhere in more detail.

When the external field reaches the critical value H_{cr1} and is then reduced to zero, the remanent magnetization exhibits a nonzero value because both DWs are now magnetized in the same direction [Fig. 4(e)]. With an increasing field in the opposite direction—see the blue curve in Fig. 4(g) for negative H_{ext}—the system undergoes the same sequence of transitions: first into the state with HBL at $|H_{ext}| = H_{cr2}$ and after that into the field-aligned state at $|H_{ext}| = H_{cr1}$. Note that this time, the transitions take place in both domain walls simultaneously. The two peaks in the differential susceptibility, $\partial M/\partial H_{ext}$, allow us to identify the exact values of the critical fields. The dependence of H_{cr1} and H_{cr2} on the interlayer exchange coupling, k_{IEC}, is shown in Fig. 4(h). For $k_{IEC} = 0.18$, the theoretically determined H_{cr1} and H_{cr2} are maximally close to the experimentally measured values. We therefore conclude that

with $A = 8$ pJ/m and $k_{\mathrm{IEC}} = 0.18$, our theoretical model describes the main features of the physical processes taking place in the experiment.

The above theoretical model assumes a perfect crystal structure without any defects, grain boundaries, and other variations of the coupling constants that are inevitably present in samples prepared by magnetron sputter deposition. Because of that, the shapes of the theoretical and experimental magnetization curves differ in some details. For instance, the magnetization at H_{cr1} in the theoretical curve of Fig. 4(g) exhibits an abrupt jump while, in the experimental curves, it shows a nearly continuous transition. Moreover, the ideal crystal model cannot explain the opening of minor magnetization loops seen in Figs. 3(a)–3(c). Below, we show that these discrepancies can be omitted at least on a qualitative level, assuming that the multilayer has a certain distribution of the interlayer exchange coupling, k_{IEC}, over the film area. The green curve, $\varphi(k_{\mathrm{IEC}})$, in Fig. 4(h) shows the probability density function for a normal distribution with the mean $\mu = 0.18$ and variance $\sigma^2 = 0.01$. The inset in Fig. 5 shows the probability P as a function of k_{IEC} on a discrete mesh with $\Delta k_{\mathrm{IEC}} = 0.02$. The probability P here means the percentage of stripes that belong to the structural region with a particular k_{IEC}. For each value of k_{IEC} with the step Δk_{IEC}, we calculate two minor-loop magnetization curves with the maximal fields $\mu_0 H_m = 0.3$ T and 0.15 T. The averaged magnetization at each value of the external field is calculated from

$$M(H_{\mathrm{ext}}) = \sum_i P_i M_i(H_{\mathrm{ext}}), \tag{3}$$

where the summation runs over all intervals of k_{IEC} and P_i denotes the probability for the ith interval. The averaged magnetization curves are shown in Fig. 5. Since for small k_{IEC} the critical field H_{cr1} is small and the probability for the transition into the field-aligned state is nonzero, the resulting magnetization curves in both cases for $\mu_0 H_m = 0.3$ T and 0.15 T have nonzero remanent magnetization. For $\mu_0 H_m = 0.3$ T, the magnetization curve near H_{cr1} has a quite smooth behavior and fits the shape of the experimental curves better than the curve of Fig. 4(g).

Besides variations of interlayer exchange coupling in the real samples, other parameters—such as, for instance, the anisotropy strength and the anisotropy direction—might have their own distributions. Because of that, the above simulations do not provide an exact quantitative agreement with the experimentally measured magnetization curves. Nevertheless, these simulations clearly reveal that the presence of certain types of defects may trigger the transition from a DW with HBL into a field-aligned state even at a low magnetic field, $H_{\mathrm{ext}} \ll H_{\mathrm{cr1}}$.

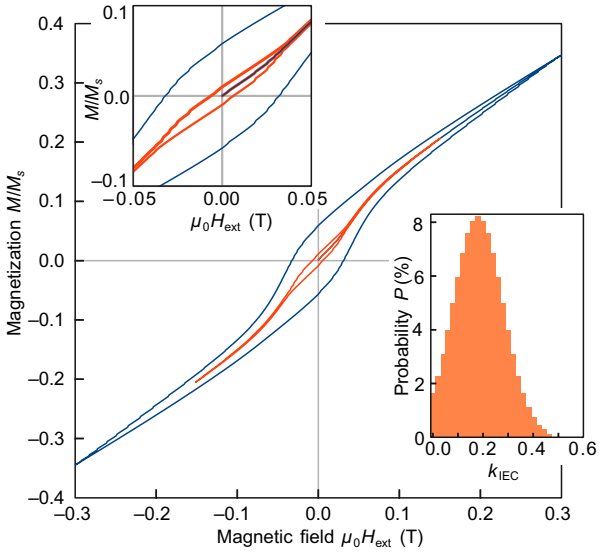

FIG. 5. The minor-loop magnetization curve above (blue) and below (red) the H_{cr1}, calculated assuming a normal distribution of exchange coupling over the $X = 48$ sample. The top inset shows an enlarged view of the magnetization curves near remanence. The bottom inset displays the probability distribution for the parameter k_{IEC}, representing the interlayer exchange coupling between adjacent Co layers. The mean of the distribution corresponds to $k_{\mathrm{IEC}} = 0.18$.

V. DISCUSSION

From the quantitative agreement of the critical fields and the qualitative agreement of the experimental and theoretical magnetization curves, we conclude that the most realistic picture of the physical processes taking place during the application of in-plane magnetic fields along the stripe domains looks as follows. The critical field H_{cr1} corresponds to the transition of all DWs into the field-aligned state. This explains the maximal remanent magnetization after the application of an external field exceeding H_{cr1}. However, the transition of some individual DWs into the energetically favorable field-aligned state takes place even at lower external fields. The defects distributed over the volume of the sample, weak variations of exchange or anisotropy, as well as thermal fluctuations represent triggers for such transitions. These events are rare at weak fields below H_{cr2} because the energy barrier is larger. This explains the first plateau in the $M_r(H_m)$ curve [Fig. 3(d)]. When H_m approaches the critical field H_{cr2}, the HBLs are formed in the DWs with opposite magnetization to the external field. In the ac-demagnetized state, approximately half of the DWs belong to this category, resulting in a total $M_r = 0$. For an ideal defect-free crystal, the DWs with HBL can survive up to H_{cr1} but due to the presence of defects, some portion of the DWs switches to the field-aligned state as soon as HBLs are formed (at about H_{cr2}). That happens because of the high magnetization gradients in the DWs with HBL, which makes them sensitive to the presence of the defects.

Denoting by n_+ and n_- the number of DWs polarized along and, respectively, against the previously applied field and assuming that the total number of DWs $n_+ + n_-$ is constant, the remanent in-plane magnetization along the stripe axis reads

$$\frac{M_r}{M_s} = \frac{n_+ - n_-}{n_+ + n_-}\frac{M_r^{\max}}{M_s}, \tag{4}$$

where $M_r^{\max}$ is the maximal remanent magnetization. From the relative height of the plateau in the $M_r(H_m)$ curve [Fig. 3(d)] and Eq. (4), we estimate that for $X = 48$ about 23% of the antiparallel to the field-polarized DWs undergo a switching at H_{cr2}. The collective switching of all remaining antiparallel DWs into the field-aligned state at about H_{cr1} leads to the second large step in the curve shown in Fig. 3(d). With increasing the thickness, the relative number of DWs undergoing this transition is almost unchanged. For $X = 100$ and $X = 150$, we estimate that approximately 27% and approximately 30% of the DWs, respectively, switch at H_{cr2}. The negligible thickness dependence is not surprising, as the MLs are synthesized under almost identical conditions and the small number of switching events at low field indicates the high quality of the samples. Thereby, at the critical field H_{cr2}, two processes take place: the appearance of HBL in the DWs with opposite to the field magnetization and partial switching of such DWs into the field-aligned state due to the presence of defects.

An interesting aspect revealed by the micromagnetic simulations is the hysteretic behavior of the DWs with HBL, as illustrated in Fig. 6. For a stripe-domain state with its micromagnetically determined equilibrium period, we perform simulations starting with the state at a magnetic field, $\mu_0 H_{ext} = 180$ mT, being in between H_{cr2} and H_{cr1}. The simulated domain contains four DWs, as shown in Fig. 6(a). For three of the four DWs, the Bloch component is aligned along the field, while for the other DW it is opposite to the field, thus leading to the formation of a HBL. The simulated magnetization curves for decreasing the field to zero and then increasing it back to 180 mT for samples of different thickness are shown in Fig. 6(b). Within a certain ML-thickness regime, the curves show a thickness-dependent opening, which can be defined with two critical fields, H^*_{cr2} and H_{cr2}, corresponding to the switching field of the descending and, respectively, ascending branch. Note that the critical field H_{cr2} coincides with the previous definition [indicated in Fig. 4(g)]. Figure 6(c) shows the dependence of the critical fields H^*_{cr2} and H_{cr2} on the ML thickness. According to the simulation result, below $X = 50$, the formation of the HBL represents a fully reversible process, while for thicker MLs the hysteretic behavior emerges, with an increasingly more pronounced hysteresis. For very thick MLs, the simulations predict that DWs with HBL can be stable even at zero field, such that a reverse magnetic field is required for unwinding. We confirm the theoretical prediction for the opening of minor loops near H_{cr2} by experimental measurements [see the insets in Figs. 3(a)–3(c)]. It is seen that the magnetization curve is indeed hysteresis free for $X = 48$ and that the opening increases with the film thickness. From above, we conclude that the theoretical picture based on the appearance of HBL is correct.

Still, we would like to note that full quantitative agreement between simulation and experiment is not attained, as the simulated remanent magnetizations are about half the experimental values. We identify a few reasons for this discrepancy. First, we note that the period of the experimentally aligned stripe domains via in-plane demagnetization might be lower than the actual ground-state equilibrium period. In particular, the period of a labyrinth domain pattern obtained after out-of-plane demagnetization typically shows a periodicity

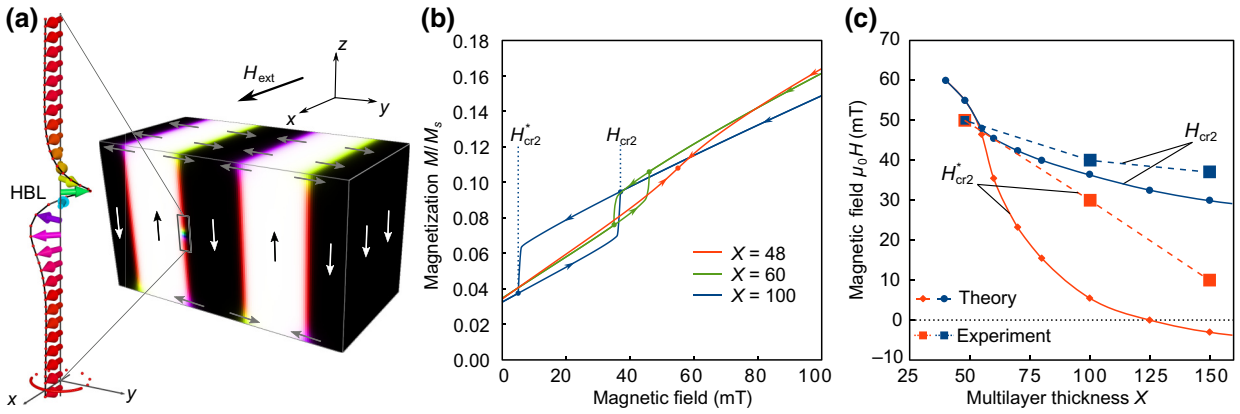

FIG. 6. (a) The simulated domains for $X = 100$ containing two periods of stripe domains separated by three DWs polarized along the external field and one DW with HBL. (b) The minor magnetization loops for MLs of different thickness simulated for the system (a). (c) The dependence of the critical fields H_{cr2} and H^*_{cr2} defining the opening of the minor loop as functions of the ML thickness.

approximately up to 50% larger than for aligned stripe domains [29,39]. It has been suggested recently that the labyrinth pattern in magnetic MLs is closer to the ground-state equilibrium period than the aligned stripe-domain pattern, because the formation of the latter via in-plane demagnetization might be more susceptible to defects [39]. As follows from Fig. 4(f), a higher periodicity corresponds to higher exchange stiffness and, as a result, a larger width of DWs, such that a higher in-plane magnetization might be obtained in the simulations. Additionally, there might be a perpendicular anisotropy gradient present as the average out-of-plane lattice spacing relaxes from an initially strained state (due to the Pt seed layer) to its equilibrium value, similar to what has been observed in recent studies [40] for MLs with $X > 20$.

VI. CONCLUSIONS

We study the DW-magnetization switching in aligned stripe-domain states in $[(\mathrm{Co}(0.44\ \mathrm{nm})/\mathrm{Pt}(0.7\ \mathrm{nm})]_X$ ($X =$ 48, 100, 150) multilayers with perpendicular magnetic anisotropy. While no remanent in-plane moment is present in the in-plane ac-demagnetized state, we are able to induce a net remanent moment after the application of an in-plane magnetic field parallel to the stripes. We demonstrate that this in-plane moment originates from the polarization of the Bloch-type DWs. The DW polarization as well as its full reversal have no influence on the stripe-domain alignment and morphology itself. This permits the study of the DW-magnetization reversal by recording the remanent magnetization after the application of different magnetic field amplitudes (H_m) along the stripe-domain direction. The reversal process shows a double-step behavior with the DW activation field (H_{cr2}) and DW saturation field (H_{cr1}), as listed in Table I. The reversal mechanism is attributed to a DW-magnetization twist in localized regions, similar to HBLs introduced by Malozemoff and Slonczewski for garnet films [20]. At H_{cr2}, the HBLs emerge in DWs polarized opposite to the applied field. Some percentage of these DWs then undergoes a possibly defect-induced switching, yielding a net remanent moment when reducing the field back to 0. At H_{cr1}, finally, all HBLs collapse, resulting in full polarization of the DWs and maximal remanent moment. This transition, however, is smoothed in the hysteresis loops due to film inhomogeneities.

Our studies provide the opportunity for the experimental estimation of the effective DW width using only magnetometry and conventional magnetic force microscopy methods. For $Q \gtrsim 1$, the effective DW width is practically independent of the ML thickness. Furthermore, the DW-magnetization switching at small external fields, opens a pathway to control the DW magnetization with high precision independent of the domain pattern. Possibly, the DW-magnetization switching might be also achieved using a spin-polarized electric current. This, however, requires further investigations.

Our results are relevant for studies of recently discovered magnetic multilayers with IDMI [3,13,41,42]. It is argued that the IDMI term supports the Néel component of the DW being preferred over the Bloch component with some intermediate or hybrid states, depending on the IDMI strength [43,44]. For high-Q materials, the in-plane remanent moment, measured parallel to the DW direction, should be characteristic for the portion of the Bloch component. The Néel-type modulations inside the DW in ML with IDMI should provide zero remanent magnetization in the plane of the film. We note that a possible small IDMI due to a slight sputter-growth-induced asymmetry of the interfaces at individual Co layers in our samples cannot be excluded [45]. The substantial remanent magnetization, however, indicates that the Néel-type modulations induced by IDMI are negligible.

Lastly, the control of the DW polarization in magnetic parallel stripe-domain configurations can be applied in magnonics, where the stripe DWs themselves are used as an effective medium and channel for spin-wave propagation, resembling a self-organized magnonic crystal [6–9,17]. It has, for example, been shown in Ref. [7] that an alternating Bloch-wall polarization in a parallel stripe-domain structure leads to less strong spin-wave mode separation as compared to Bloch walls with the same polarization. Thus the band gaps between different magnon mode families in parallel stripe-domain patterns can effectively be tuned and altered by alignment of the Bloch-type domain walls. This opens up the possibility of "reprogramming" the magnonic band structure in such self-organized magnonic crystals based on parallel stripe-domain systems.

ACKNOWLEDGMENTS

We are grateful to Thomas Naumann and Jakob Heinze for experimental and technical support. N.S.K., B.R., and S.S. gratefully acknowledge financial support through the Priority Program SPP2137 "Skyrmionics" of the German Research Foundation (DFG) within Projects No. KI 2078/1-1, No. RE-1164/6-1, and No. LU-2261/2-1.

[1] M. S. Pierce, J. E. Davies, J. J. Turner, K. Chesnel, E. E. Fullerton, J. Nam, R. Hailstone, S. D. Kevan, J. B. Kortright, Kai Liu, L. B. Sorensen, B. R. York, and O. Hellwig, Influence of structural disorder on magnetic domain formation in perpendicular anisotropy thin films, Phys. Rev. B **87**, 184428 (2013).

[2] C.-H. Lambert, S. Mangin, B. S. D. Ch. S. Varaprasad, Y. K. Takahashi, M. Hehn, M. Cinchetti, G. Malinowski,

K. Hono, Y. Fainman, M. Aeschlimann, and E. E. Fullerton, All-optical control of ferromagnetic thin films and nanostructures, Science **345**, 1337 (2014).

[3] A. Fert, N. Reyren, and V. Cros, Magnetic skyrmions: Advances in physics and potential applications, Nat. Rev. Mater. **2**, 17031 (2017).

[4] S. Mangin, D. Ravelosona, J. A. Katine, M. J. Carey, B. D. Terris, and E. E. Fullerton, Current-induced magnetization reversal in nanopillars with perpendicular anisotropy, Nat. Mater. **5**, 210 (2006).

[5] A. Hirohata and K. Takanashi, Future perspectives for spintronic devices, J. Phys. D: Appl. Phys. **47**, 193001 (2014).

[6] Ch. Benerjee, P. Gruszecki, J. W. Klos, O. Hellwig, M. Krawczyk, and A. Barman, Magnonic band structure in a Co/Pd stripe domain system investigated by Brillouin light scattering and micromagnetic simulation, Phys. Rev. B **96**, 024421 (2017).

[7] P. Gruszecki, Ch. Banerjee, M. Mruczkiewicz, O. Hellwig, A. Barman, and M. Krawczyk, The influence of the internal domain wall structure on spin wave band structure in periodic magnetic stripe domain patterns, Solid State Phys. **70**, 79 (2019).

[8] I. S. Camara, S. Tacchi, L.-C. Garnier, M. Eddrief, F. Fortuna, G. Carlotti, and M. Marangolo, Magnetization dynamics of weak stripe domains in Fe-N thin films: A multitechnique complementary approach, J. Phys.: Condens. Matter **29**, 465803 (2017).

[9] Y. Henry, D. Stoeffler, J.-V. Kim, and M. Bailleul, Unidirectional spin-wave channeling along magnetic domain walls of Bloch type, Phys. Rev. B **100**, 024416 (2019).

[10] T. Vemulkar, R. Mansell, D. C. M. C. Petit, R. P. Cowburn, and M. S. Lesniak, Highly tunable perpendicularly magnetized synthetic antiferromagnets for biotechnology applications, Appl. Phys. Lett. **107**, 012403 (2015).

[11] K. Chesnel, A. S. Westover, C. Richards, B. Newbold, M. Healey, L. Hindman, B. Dodson, K. Cardon, D. Montealegre, J. Metzner, T. Schneider, B. Böhm, F. Samad, L. Fallarino, and O. Hellwig, Morphological stripe-bubble transition in remanent magnetic domain patterns of Co/Pt multilayer films and its dependence on Co thickness, Phys. Rev. B **98**, 224404 (2018).

[12] L. Fallarino, A. Oelschlägel, J. A. Arregi, A. Bashkatov, F. Samad, B. Böhm, K. Chesnel, and O. Hellwig, Control of domain structure and magnetization reversal in thick Co/Pt multilayers, Phys. Rev. B **99**, 024431 (2019).

[13] A. Soumyanarayanan, M. Raju, A. L. G. Oyarce, A. K. C. Tan, M.-Y. Im, A. P. Petrović, P. Ho, K. H. Khoo, M. Tran, C. K. Gan, F. Ernult, and C. Panagopoulos, Tunable room-temperature magnetic skyrmions in Ir/Fe/Co/Pt multilayers, Nat. Mat. **16**, 898 (2017).

[14] M. Jamali, K. Narayanapillai, X. Qiu, L. M. Loong, A. Manchon, and H. Yang, Spin-Orbit Torques in Co/Pd Multilayer Nanowires, Phys. Rev. Lett. **111**, 246602 (2013).

[15] K.-F. Huang, D.-S. Wang, H.-H. Lin, and C.-H. Lai, Engineering spin-orbit torque in Co/Pt multilayers with perpendicular magnetic anisotropy, Appl. Phys. Lett. **107**, 232407 (2015).

[16] M. Shahzadeh, O. Andrievska, R. Salikhov, L. Fallarino, O. Hellwig, and S. Pisana, Nondiffusive transport and anisotropic thermal conductivity in high-density Pt/Co superlattices, ACS Appl. Electron. Mater. **3**, 1931 (2021).

[17] Ch. Liu *et al.*, Current-controlled propagation of spin waves in antiparallel, coupled domains, Nat. Nanotech. **14**, 691 (2019).

[18] S. Fin, R. Tomasello, D. Bisero, M. Marangolo, M. Sacchi, H. Popescu, M. Eddrief, C. Hepburn, G. Finocchio, M. Carpentieri, A. Rettori, M. G. Pini, and S. Tacchi, In-plane rotation of magnetic stripe domains in $Fe_{1-x}Ga_x$ thin films, Phys. Rev. B **92**, 224411 (2015).

[19] L.-C. Garnier, M. Marangolo, M. Eddrief, D. Bisero, S. Fin, F. Casoli, M. G. Pini, A. Rettori, and S. Tacchi, Stripe domains reorientation in ferromagnetic films with perpendicular magnetic anisotropy, J. Phys. Mater. **3**, 024001 (2020).

[20] A. P. Malozemoff and J. C. Slonczewski, *Magnetic Domain Walls in Bubble Materials* (Academic Press, New York, 1979).

[21] A. Hubert and R. Schäfer, *Magnetic Domains* (Springer, Berlin, 2009), p. 235

[22] C. Kittel, Theory of the structure of ferromagnetic domains in films and small particles, Phys. Rev. **70**, 965 (1946).

[23] F. Virot, L. Favre, R. Hayn, and M. D. Kuz'min, Theory of magnetic domains in uniaxial thin films, J.Phys. D: Appl. Phys. **45**, 405003 (2012).

[24] P. Novotny, R. Gemperle, L. Murtinova, and J. Kaczer, Experimental evidence of the magnetic moment of Bloch walls in garnet films, J. Magn. Magn. Mater. **68**, 379 (1987).

[25] P. Novotny and R. Gemperle, Double-jump magnetization reversal process in the domain walls of garnet films, J. Magn. Magn. Mater. **102**, 18 (1991).

[26] K. Patek, R. Gemperle, L. Murtinova, and J. Kaczer, Magnetization reversal and Bloch lines in bubble domain walls, J. Magn. Magn. Mater. **123**, 223 (1993).

[27] A. Gemperle, R. Gemperle, and P. Novotny, Transmission electron microscopy investigation of stripe domain walls in cobalt foils in in-plane fields, J. Magn. Magn. Mater. **129**, 410 (1994).

[28] J. E. Davies, O. Hellwig, E. E. Fullerton, G. Denbeaux, J. B. Kortright, and K. Liu, Magnetization reversal of Co/Pt multilayers: Linking macroscopic and microscopic level, Phys. Rev. B **70**, 224434 (2004).

[29] O. Hellwig, G. P. Denbeaux, J. B. Kortright, and E. E. Fullerton, *X*-ray studies of aligned magnetic stripe domains in perpendicular multilayers, Phys. B **336**, 136 (2003).

[30] O. Hellwig, A. Berger, J. B. Kortright, and E. E. Fullerton, Domain structure and magnetization reversal of antiferromagnetically coupled perpendicular anisotropy films, J. Magn. Magn. Mater. **319**, 13 (2007).

[31] M. Labrune and L. Belliard, Stripe domains in multilayers: Micromagnetic simulations, Phys. Stat. Sol. (a) **174**, 483 (1999).

[32] H. Niedoba and M. Labrune, Magnetization reversal via Bloch points nucleation in nanowires and dots: A micromagnetic study, Eur. Phys. J. B **47**, 467 (2005).

[33] E. E. Fullerton, J. S. Jiang, M. Grimsditch, C. H. Sowers, and S. D. Bader, Exchange-spring behavior in epitaxial hard/soft magnetic bilayers, Phys. Rev. B **58**, 193 (1997).

[34] E. E. Fullerton, J. S. Jiang, and S. D. Bader, Hard/soft magnetic heterostructures: Model exchange-spring magnets, J. Magn. Magn. Mater. **200**, 392 (1999).

[35] O. Hellwig, J. B. Kortright, K. Takano, and E. E. Fullerton, Switching behavior of Fe-Pt/Ni-Fe exchange-spring films studied by resonant soft-x-ray magneto-optical Kerr effect, Phys. Rev. B **62**, 694 (2000).

[36] I. Lemesh, F. Büttner, and G. S. D. Beach, Accurate model of stripe domain phase of perpendicularly magnetized multilayers, Phys. Rev. B **95**, 174423 (2017).

[37] A. Vansteenkiste, J. Leliaert, M. Dvornik, M. Helsen, F. Garcia-Sanchez, and B. Van Waeyenberge, The design and verification of MUMAX^3, AIP Adv. **4**, 10 (2014).

[38] J.-H. Shim, A. A. Syed, Y. Shin, J.-W. Kim, H.-G. Piao, S.-H. Lee, K. M. Lee, J.-R. Jeong, D.-H. Kim, and D. E. Kim, Ultrafast dynamics of exchange stiffness in Co/Pt multilayer, Commun. Phys. **3**, 74 (2020).

[39] A. G. Kozlov, A. G. Kolesnikov, M. E. Stebliy, A. P. Golikov, and A. V. Davydenko, Domain-period method for determination of the energy of the Dzyaloshinskii-Moriya interaction in [Co/Pd(111)]5 superlattices, Phys. Rev. B **102**, 144411 (2020).

[40] L. Fallarino, S. Stienen, R. A. Gallardo, J. A. Arregi, V. Uhlíř, K. Lenz, R. Hübner, A. Oelschlägel, O. Hellwig, and J. Lindner, Higher-order ferromagnetic resonances in out-of-plane saturated Co/Au magnetic multilayers, Phys. Rev. B **102**, 094434 (2020).

[41] G. Yu, P. Upadhyaya, Q. Shao, H. Wu, G. Yin, X. Li, C. He, W. Jiang, X. Han, P. Kh. Amiri, and K. L. Wang, Room-temperature skyrmion shift device for memory application, Nano Lett. **17**, 261 (2017).

[42] M. He, G. Li, Zh. Zhu, Y. Zhang, L. Peng, R. Li, J. Li, H. Wei, T. Zhao, X.-G. Zhang, Sh. Wang, S.-Z. Lin, L. Gu, G. Yu, J. W. Cai, and B.-g. Shen, Evolution of topological skyrmions across the spin reorientation transition in Pt/Co/Ta multilayers, Phys. Rev. B **97**, 174419 (2018).

[43] W. Legrand, J.-Y. Chauleau, D. Maccariello, N. Reyren, S. Collin, K. Bouzehouane, N. Jaouen, V. Cros, and A. Fert, Hybrid chiral domain walls and skyrmions in magnetic multilayers, Sci. Adv. **4**, eaat0415 (2018).

[44] I. Lemesh and G. S. D. Beach, Twisted domain walls and skyrmions in perpendiculary magnetized multilayers, Phys. Rev. B **98**, 104402 (2018).

[45] S.-G. Je, D.-H. Kim, S.-C. Yoo, B.-C. Min, K.-J. Lee, and S.-B. Choe, Asymmetric magnetic domain-wall motion by the Dzyaloshinskii-Moriya interaction, Phys. Rev. B **88**, 214401 (2013).